J. Fluid Mech. (1999), *vol.* 381, *pp.* 357–380. Printed in the United Kingdom

Large-eddy simulation of boundary-layer transition on a swept wedge

By XIAOLI HUAI[1]†, RONALD D. JOSLIN[2] AND UGO PIOMELLI[1]

[1]Department of Mechanical Engineering, University of Maryland, College Park, MD 20742, USA

[2]Fluid Mechanics and Acoustics Division, NASA Langley Research Center, Mail Stop 170, Hampton, VA 23681-0001, USA

(Received 8 May 1997 and in revised form 22 September 1998)

The spatial evolution of the disturbances that lead to boundary-layer transition on a swept wedge is computed by large-eddy simulations (LES). Stationary and travelling crossflow-vortex disturbances are generated using steady and random-amplitude suction and blowing on the wedge. For a fixed initial amplitude of the stationary vortex and low-amplitude unsteady disturbances, the LES show the evolution of stationary-dominated crossflow disturbances similar to previous simulations and experiments: linear amplification is followed by vortex roll-over and doubly inflectional velocity profiles just prior to transition. A high-frequency secondary instability is associated with the double inflection points in the velocity profiles. The harmonic modes of the primary disturbance were found to be amplified, while no energy was found in any subharmonic mode. The physical phenomena were significantly different when the stationary and travelling vortices have comparable initial amplitudes: in this case, the vortex roll-over does not occur and transition is dominated by the travelling-wave component.

1. Introduction

The state of the three-dimensional boundary-layer flow on the wings and fuselage of an aircraft determines the viscous drag contribution to the total drag of the aircraft, which is dependent on the flow state, and can equal 40% to 50% of the total drag (Arcara, Bartlett & McCullers 1991). A reduction in viscous drag can lead to reduced fuel expenditures, reduced emission (pollution), reduced aircraft size or enhanced range, and reduced noise. Laminar flow is preferable to turbulent flow (except in recovery regions where the pressure-drag penalty of boundary-layer separation is severe) because the significantly lower skin friction of laminar flow leads to decreased viscous drag.

Obtaining laminar flow on swept wings, however, requires careful attention to the design, manufacturing, and operation of the aircraft. Surface waves or irregularities on the wing can 'trip' the boundary layer, and turbulent contamination that results from wing/fuselage junctures can lead to boundary-layer transition close to the leading edge of the wing. For long-spanned aircraft, travelling waves can become unstable along the attachment line (which is located near the leading edge) and

† Present address: AEA Technology Engineering Software Inc., 2000 Oxford Drive, Pittsburgh, PA, 15102, USA.

cause transition there. Several mechanisms may be at play. Itoh (1996) discussed the existence of a new instability present in regions of large streamline curvature (near the attachment line of a wing, for instance). As the curvature decreases, however, the critical Reynolds number for this instability approaches infinity. The region covered in the present paper has mild streamline curvature and, therefore, the streamline-curvature instability will have little impact on the flow. Lingwood (1997) has shown that swept-wedge flow is absolutely unstable in the chordwise direction; the role of this instability versus the convective instabilities in the transition process is not currently known. Near the mid-chord region of a wing or when the flow is not strongly accelerated, two-dimensional transition phenomena are important. Depending on wing sweep and pressure gradient, a boundary layer can be susceptible to crossflow-vortex instabilities, which are caused by the inflection point present in the velocity profile perpendicular to the streamline velocity component within the boundary layer. For accelerating flows and highly swept wings ($> 25^\circ$), these crossflow-vortex instabilities are unavoidable (without flow control) and can cause transition to occur within a few percent chord. Significant research has been conducted toward understanding the linear amplification and nonlinear interaction of crossflow disturbances during the transition process; crossflow-dominated transition is the focus of this paper.

Many experiments over the last decade have led to increased understanding of the crossflow-dominated transition problem by highlighting a decreased role of the Tollmien–Schlichting disturbances, compared with two-dimensional boundary layers. For example, using a pressure gradient to suppress Tollmien–Schlichting instabilities, both stationary and travelling crossflow vortices have been observed experimentally by Arnal, Coustols & Juillen (1984), Bippes & Nitschke-Kowsky (1987), Müller & Bippes (1988), Dagenhart *et al.* (1990), Dagenhart (1992), and Reibert *et al.* (1996). Müller & Bippes (1988) and Bippes, Müller & Wagner (1991) showed that travelling crossflow vortices may have smaller or larger initial energy for low- and high-disturbance tunnels, respectively, whereas travelling disturbances become very important in high-disturbance tunnels. For stationary-vortex-dominated flow, Dagenhart *et al.* (1990) observed doubly inflectional velocity profiles and a phenomenon called 'vortex roll-over'; the inflectional profiles lead to higher-frequency secondary-instability travelling modes (Kohama, Saric & Hoos 1991). Experiments also showed that unsteady disturbances, especially the secondary-instability modes, play an important role in driving the laminar flow to transition and turbulence (Müller & Bippes 1988). More recently, Lerche (1996) studied the transition process on a swept wedge using an oscillating membrane to initiate travelling modes, and surface roughness to introduce stationary modes. A high-frequency (2 kHz) instability was detected about midway through the boundary layer in the region of vortex saturation. Similar to previous studies, Lerche (1996) looked at the phase relationship between the high-frequency mode and the primary mode to conclude that the high-frequency secondary mode is linked to the mean flow inflection points and negative local mean velocities. Finally, Deyhle & Bippes (1996) studied the impact of environmental conditions on the stationary and travelling instability development in the wind tunnel. They note that the initial amplitudes of the stationary vortices depend on the surface conditions, while the initial amplitudes of the travelling modes depend on both the surface conditions and unsteady free-stream conditions. It was demonstrated that sound does not affect the formation of crossflow disturbances in the three-dimensional boundary layer.

Using linear stability theory to compute the amplification of crossflow disturbances, Dallman & Bieler (1987) showed that travelling vortices are more unstable than stationary crossflow vortices. Fischer & Dallman (1988) and Balachandar, Streett &

Malik (1990) used secondary instability theory to predict the growth of the secondary modes arising from the influence of the primary crossflow vortex instability on the base flow. As the disturbances become finite in amplitude, and mean-flow distortion occurs, however, the linear and quasi-linear theories are no longer valid.

Bertolotti & Crouch (1992), Malik, Li & Chang (1994), and Haynes & Reed (1996) have used the parabolized stability equations (PSE) to predict the nonlinear features of transition on swept wings. Bertolotti & Crouch (1992) showed results from the coupling of receptivity theory with PSE theory for use in transition prediction. The computational results of Malik *et al.* (1994) for crossflow disturbance evolution in swept Hiemenz flow (Hall, Malik & Poll, 1984) were shown to capture the evolution of the disturbance up to the weakly nonlinear stage of development. The computational results of Haynes & Reed (1996) for the nonlinear evolution of stationary crossflow disturbances agree with the experiments of Reibert *et al.* (1996) as the dominantly stationary vortices reach saturation. A potential explanation of this saturation feature of the vortices was offered by Gajjar (1996), who conjectured that the long-wavelength crossflow disturbances are governed by the unsteady nonlinear critical-layer equations, and proposed that such equations can lead to growth rates of the disturbance being driven to zero; hence, the saturation of crossflow disturbances may be explained by this critical-layer nonlinearity.

The direct numerical simulation (DNS) approach, in which the Navier–Stokes equations are solved with no approximation within a temporal or spatial framework (the spatial framework being more expensive, but more physically realistic), has also been used to investigate the relationships between the multiple modes in the swept-wing boundary-layer flow for simple geometries. Using the Falkner–Skan–Cooke (FSC) similarity solution (Falkner & Skan 1931; Cooke 1950), Meyer & Kleiser (1988, 1990) performed a temporal DNS of crossflow disturbance evolution on swept wedges (the wing surface curvature was ignored). Although boundary-layer growth is neglected and spatial periodicity is assumed with the temporal formulation, Meyer & Kleiser (1988) captured the qualitative features of the transition process up to the nonlinear interaction stage, and Müller, Bestek & Fasel (1993, 1996) showed a good comparison between DNS and experimental velocity profiles in the linear regime and studied the interaction between a stationary vortex and a single travelling mode. Using the fringe-method, Spalart (1990) computed the evolution of crossflow disturbances in swept Hiemenz flow. Joslin & Streett (1994) and Joslin (1995) performed spatial DNS calculations to compute the linear and nonlinear evolution of stationary crossflow vortices in swept-wedge flow. Similarly to the experiments, the stationary vortex evolution was marked by a region of linear amplification, vortex alignment approximately in the streamline direction, doubly inflectional velocity profiles in the large-amplitude region, and the vortex roll-over phenomena.

In summary, the experimental and computational studies have shown that:

(*a*) The stationary vortices are initiated by surface roughness (Deyhle & Bippes 1996).

(*b*) These vortices are aligned within a few degrees of the streamline (Meyer & Kleiser 1988).

(*c*) In low-disturbance tunnels, stationary vortices lead to vortex roll-over, inflectional profiles, and dominate transition (Dagenhart *et al.* 1990).

(*d*) The inflectional velocity profiles can generate high-frequency, secondary-instability travelling modes (Kohama *et al.* 1991).

(*e*) In high-disturbance tunnels, travelling disturbances dominate transition (Bippes *et al.* 1991).

(*f*) PSE theory, temporal DNS, and spatial DNS capture the linear and nonlinear evolution of stationary crossflow-vortex disturbances (Malik *et al.* 1994; Meyer & Kleiser 1988; Joslin & Streett 1994).

Despite many theoretical and experimental studies and some DNS and PSE studies, however, the current understanding of transition in a swept-wing boundary layer is still incomplete: while much is known about the stationary-dominated crossflow transition case, very little is still known about stationary/travelling disturbance interaction and breakdown (Kachanov 1996). For this reason, the present study is focused on studying the interaction of stationary and unsteady disturbances. The investigation will be conducted using large-eddy simulation (LES), since capturing the large scales and modelling the subgrid scales decreases significantly the cost of the numerical solution of turbulent and transitional flow problems, compared with DNS. DNS has not been used to study unsteady swept-wing transition because of its enormous cost (125 CRAY-2 CPU hours were required for the stationary crossflow study by Joslin & Streett 1994). Even using LES, as will be seen later, the computational effort due to the grid resolution requirements was extreme, to the point that, although a grid refinement study was conducted, it was not possible to reach truly grid-invariant solutions. It will be shown, however, that the finest grid used gives reliable results.

For a fixed stationary disturbance, simulations are conducted with small- and large-amplitude time-dependent disturbances. The effect of random, three-dimensional, and time-dependent disturbances on the flow breakdown, and the interaction between the stationary vortices typical of swept-wing transition and the travelling modes generated by the random disturbance are investigated.

In the following, the problem formulation and the numerical method used will be presented. Then, the numerical results will be discussed. Finally, some conclusions will be drawn.

2. Problem formulation

In large-eddy simulations, the flow variables (u_i and p) are decomposed into a large-scale (or resolved) component, denoted by an overbar, and a subgrid-scale (SGS) component, denoted by a prime:

$$f = \overline{f} + f'. \tag{2.1}$$

The large-scale component is defined by the convolution of $f(\boldsymbol{x})$ with a filter function $G(\boldsymbol{x}')$. Applying the filtering operation to the incompressible Navier–Stokes and continuity equations

$$\frac{\partial u_i}{\partial t} + \frac{\partial u_i u_j}{\partial x_j} = -\frac{\partial p}{\partial x_i} + \frac{1}{Re}\frac{\partial^2 u_i}{\partial x_j \partial x_j}; \quad \frac{\partial u_i}{\partial x_i} = 0 \tag{2.2}$$

(where the indices follow Einstein's summation convention) leads to equations governing the large-scale motions:

$$\frac{\partial \overline{u}_i}{\partial t} + \frac{\partial \overline{u}_i \overline{u}_j}{\partial x_j} = -\frac{\partial \overline{p}}{\partial x_i} - \frac{\partial \tau_{ij}}{\partial x_j} + \frac{1}{Re}\frac{\partial^2 \overline{u}_i}{\partial x_j \partial x_j}; \quad \frac{\partial \overline{u}_i}{\partial x_i} = 0, \tag{2.3}$$

where the small, unresolved-scale contributions appear through the subgrid-scale stresses $\tau_{ij} = \overline{u_i u_j} - \overline{u}_i \overline{u}_j$ that must be modelled.

In the present simulations, the Cartesian coordinate system shown in figure 1 is used, with $\boldsymbol{x} = (x, y, z)$ denoting the streamwise, wall-normal, and spanwise coordinates respectively. The equations are non-dimensionalized by the free-stream

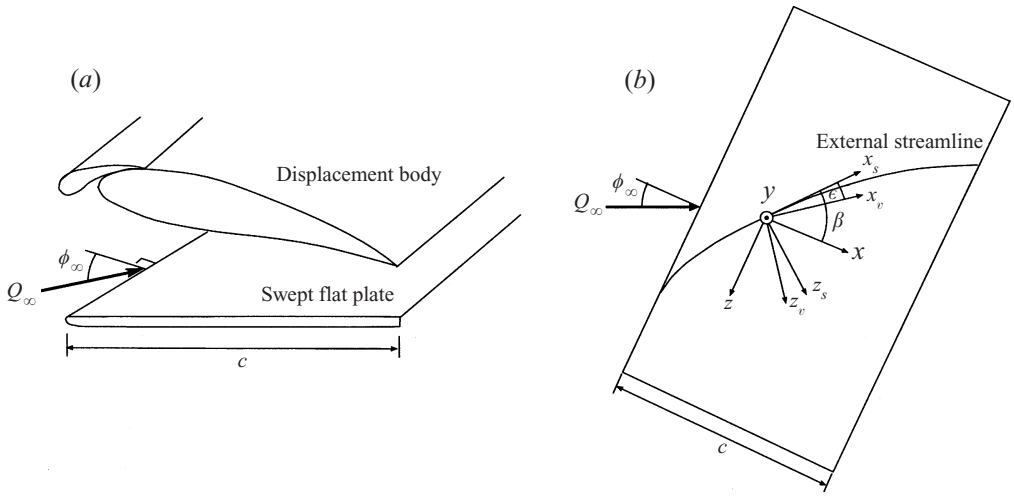

FIGURE 1. Sketch of swept-wing (*a*) experimental setup and (*b*) coordinate systems.

edge velocity $Q_{e,o}$ at the computational inflow boundary, the reference length scale $\delta_0 = (\nu x_c / U_{e,o,c})^{1/2}$ at the computational inflow boundary, and the kinematic viscosity ν. The Reynolds number is then defined as $Re = Q_{e,o}\delta_0/\nu$. Note that $U_{e,o,c}$ is the chordwise edge velocity component at the computational inflow boundary. Curvature is neglected.

The instantaneous large-scale velocity $\overline{u}_i(\boldsymbol{x}, t)$ and pressure $\overline{p}(\boldsymbol{x}, t)$ are decomposed into base, $U_{bi}(\boldsymbol{x})$ and $P_b(\boldsymbol{x})$, and disturbance, $\widetilde{u}_i(\boldsymbol{x}, t)$ and $\widetilde{p}(\boldsymbol{x}, t)$, components as

$$\overline{u}_i(\boldsymbol{x}, t) = U_{bi}(\boldsymbol{x}) + \widetilde{u}_i(\boldsymbol{x}, t) \quad \text{and} \quad \overline{p}(\boldsymbol{x}, t) = P_b(\boldsymbol{x}) + \widetilde{p}(\boldsymbol{x}, t). \tag{2.4}$$

The base flow $U_{bi}(\boldsymbol{x})$, $P_b(\boldsymbol{x})$ satisfies the steady-state Navier–Stokes and continuity equations. For three-dimensional infinite swept-wedge flows, it is given by the FSC similarity solutions, given a specified pressure gradient, sweep angle ϕ_∞, and free-stream velocity Q_∞.

By substituting equations (2.4) into (2.3) and subtracting the laminar base-flow equations, the filtered disturbance equations result:

$$\frac{\partial \widetilde{u}_i}{\partial t} + \frac{\partial \widetilde{u}_i \widetilde{u}_j}{\partial x_j} + \frac{\partial \widetilde{u}_i U_{bj}}{\partial x_j} + \frac{\partial U_{bi} \widetilde{u}_j}{\partial x_j} = -\frac{\partial \widetilde{p}}{\partial x_i} - \frac{\partial \tau_{ij}}{\partial x_j} + \frac{1}{Re}\frac{\partial^2 \widetilde{u}_i}{\partial x_j \partial x_j}; \quad \frac{\partial \widetilde{u}_i}{\partial x_i} = 0. \tag{2.5}$$

In the present simulation, the subgrid-scale stresses τ_{ij} will be modelled by the localized dynamic eddy-viscosity model proposed by Piomelli & Liu (1995). The single coefficient is computed at each point and time step, based on the energy content of the smallest resolved scales; this model has been used successfully in the simulation of turbulent, relaminarizing and transitional flows (Piomelli & Liu 1995; Huai, Joslin & Piomelli 1997), and is expected to be well suited to the study of the flow in question.

3. Solution methodology

The filtered Navier–Stokes equations were solved using the fractional-time-step method (Chorin 1968). As in the study by Joslin, Streett & Chang (1993), fourth-order finite-difference and fourth-order compact-difference schemes were used in the streamwise direction x for the pressure and the momentum equations, respectively.

Chebychev series were used in the wall-normal direction y, and Fourier series in the spanwise direction z. The implicit Crank–Nicolson time-advancement was used for the wall-normal diffusion terms and a three-stage Runge–Kutta scheme for the remaining terms (Williamson 1980). The time-step was held constant and was based on the CFL limitations of the Runge–Kutta scheme. A sharp cutoff filter was used in the wall-normal and spanwise directions whereas a box filter in real space was used in the streamwise direction.

The buffer-domain technique (Street & Macaraeg 1989) was used to treat the outflow conditions. A small non-physical buffer region is appended to the physical region of interest; in this buffer region the characteristics of the governing equations are modified to prevent reflections at the outflow boundary. The modification to the original buffer domain technique developed by Liu & Liu (1993) to reduce the required length of the buffer region was used in the present study as well.

Unphysical wave reflections resulting from physical disturbances in the flow field encountering a computational boundary can occur when boundary conditions are implemented in spatial simulations. Pruett *et al.* (1995) showed that all higher-order finite-difference schemes reflect some energy at the outflow, even when the boundary conditions applied are perfectly non-reflecting. Energy, in particular, is totally reflected for the sawtooth parasite mode, which has a wavelength $\lambda = 2\Delta x$ and is generated by the even-odd decoupling of the central-difference approximations. The reflected waves propagate upstream, and, upon encountering the Dirichlet inflow boundary, reflect again and travel downstream as spurious disturbances. This phenomenon was also observed during the present study in preliminary simulations. Rai & Moin (1991) used upwind-biased differences for the convection terms to damp the higher wavenumber content. Pruett *et al.* (1995), on the other hand, applied a low-pass, sixth-order compact-difference filter to the solution, which is equivalent to the addition of high-order numerical dissipation. Here, a fourth-order compact-difference filter (Lele 1992) was employed in the streamwise direction to remain consistent with the derivative stencil in that direction. At the downstream boundary, an explicit fourth-order filtering scheme was used to eliminate the highest wavenumber components. This approach completely filters the sawtooth wavenumber component ($k = \pi$), all other high wavenumber modes being damped to a lesser extent. The filter has no effect on low-wavenumber modes (see Huai 1996). Filtering every 10 time steps was sufficient in the present simulations.

Similarly to the simulations of subharmonic breakdown by Huai *et al.* (1997), two overlapping computational boxes (figure 2) were used to resolve the simulation in an affordable manner; forcing in the first box was accomplished by steady and unsteady suction and blowing through the wall, and the time-dependent solution near the end of the first box was used as the inflow in the second computational box.

In the first box, small-amplitude disturbances were introduced into the flow by imposing wall-normal velocity oscillations through a suction-and-blowing strip. As shown by Joslin & Streett (1994), stationary crossflow vortices can be generated with steady suction and blowing, simulating periodic surface roughness (Kachanov & Tararykin 1990). In the present study, the dominant stationary mode was explicitly introduced by applying steady suction and blowing, whereas travelling crossflow vortices were introduced through an unsteady random-noise component:

$$v(x, z, t) = A_0 f(x) g(z) + A_t f(x) R(z, t), \tag{3.1}$$

where A_0 and A_t are the amplitudes of steady and time-dependent components of the wall-normal disturbance velocity. The streamwise and spanwise suction and blowing

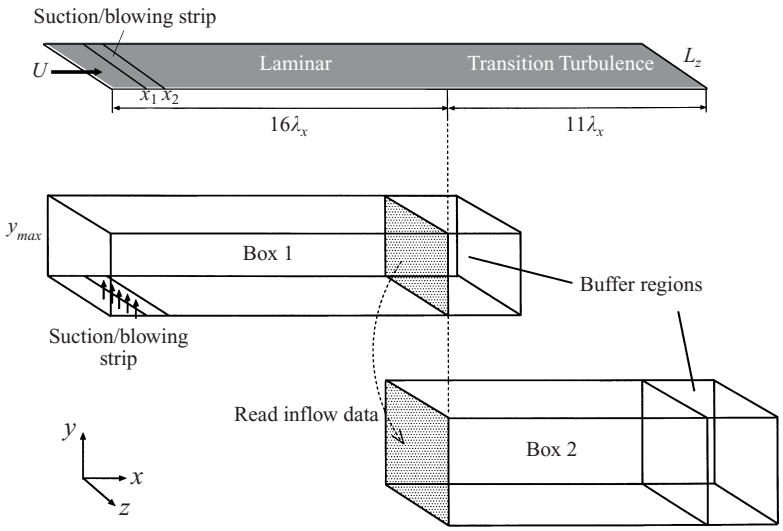

FIGURE 2. Illustration of the overlap for multiple computational boxes.

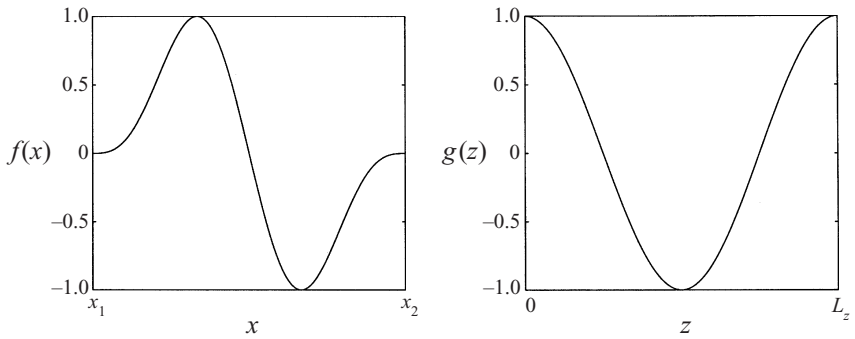

FIGURE 3. Chordwise and spanwise suction and blowing distributions.

modulation functions $f(x)$ and $g(z)$ are shown in figure 3. The unsteady components were generated using a random function $R(z,t)$ at each time step. The zero-frequency and zero-wavenumber modes of the random function were eliminated to prevent the travelling-wave component from contaminating the stationary-wave component.

After an initial transient, a time sequence of (y,z)-planes of data was stored near the end of the physical region of the computational box for two periods of the fundamental disturbance. This information was then used as an inflow boundary condition for the second computational box. Since the two periods were not sufficient to obtain stationary results in the second box, the inflow data were recycled. Since the time sequence of data may not be exactly time-periodic, a conventional windowing technique was used to prevent spurious high-frequency unsteady waves from being introduced at the inflow of the second box. Chebychev interpolation in the wall-normal direction and Fourier interpolation in the spanwise direction were used to obtain the inflow data on the finer grid of the second box. Huai (1996) and Huai *et al.* (1997) showed that the periodicity in the inflow data is lost within a few grid points of the inflow plane, and that this approach is an effective and inexpensive way to simulate boundary-layer transition.

The numerical scheme and SGS models were first validated by the simulation of the evolution of linear and nonlinear stationary crossflow disturbances on a swept wedge (Huai, Joslin & Piomelli 1994) and of boundary-layer transition on a flat plate (Huai 1996; Huai *et al.* 1997). For the stationary crossflow evolution, the LES results were in excellent agreement with the DNS results of Joslin & Streett (1994); although this comparison allowed us to validate the numerical scheme, the SGS eddy viscosity was very small at all locations (the flow was only undergoing the initial stages of transition). For the flat-plate transition problem, the LES results were in good agreement with the experimental data of Kachanov & Levchenko (1994) approaching transition and with the DNS results of Spalart (1988) in the turbulent region, where the SGS contributions were more significant.

4. Results and discussion

4.1. *Simulation parameters*

The parameters for the present simulations were chosen to complement the DFVLR swept flat-plate (wedge) experiment carried out by Müller & Bippes (1988) and the swept-wing experiments of Dagenhart (1992). Although the models were different for these experiments, both had accelerating flows and a nearly constant pressure gradient in the region of interest for the present LES study. The numeric-specific parameters were based on the DNS studies of Joslin & Streett (1994) and Joslin (1995). Based on a model sweep angle of 45° and the experimental pressure distribution by Müller & Bippes (1988), a linear pressure relation can be used to model the experiment:

$$c_p(x_c) = 0.941 - 0.845x_c. \tag{4.1}$$

As shown in figure 4, the linear fit is an accurate representation of the experimental pressure coefficient over most of the region of interest. The pressure was then used to determine solutions of the FSC base-flow equations. The computational inflow was positioned at $x_c = 0.2$. The chord length corresponded to 1.83 m and the free-stream velocity was $Q_\infty = 21.8$ m s^{-1}, resulting in a chord Reynolds number of $Re_c = 2.73 \times 10^6$; the Reynolds number at the inflow was $Re = 998$. Joslin & Streett (1994) found that with these parameters, the dominant stationary vortex mode had a spanwise wavelength of $\lambda_z = 36\delta_0$. This dominant wavelength was used to determine the spanwise domain length and the forcing wavelength.

Two simulations, denoted by LOW-T and HIGH-T, were carried out covering the chordwise regions of $0.2 < x_c < 0.54$ and $0.2 < x_c < 0.5$ respectively. They required about 100 and 90 Cray C-90 hours respectively. Tables 1(*a*) and 1(*b*) show the relevant computational parameters used for the simulations. Note that the late stages of transition are captured in box 2 only. In the tables, the domain lengths and number of grid points have the convention of streamwise × wall-normal × spanwise directions and the domain lengths are non-dimensionalized by δ_0. To obtain a measure of the grid independence, a finer resolution was also used for box 2 of the HIGH-T simulation (the fine-mesh calculation is denoted by HIGH-TF). Details of HIGH-TF are shown in table 1(*c*); the number of grid points in x was doubled and the domain length in z was decreased by one-third (since the HIGH-T calculation had shown little energy in the modes with wavelength larger than $L_z/3$) compared with the HIGH-T simulation. The HIGH-TF simulation required 175 Cray C-90 hours.

In all simulations the amplitude of the steady suction and blowing (stationary disturbance) was fixed at $A_0 = 10^{-4}$, and the amplitude of unsteady suction and

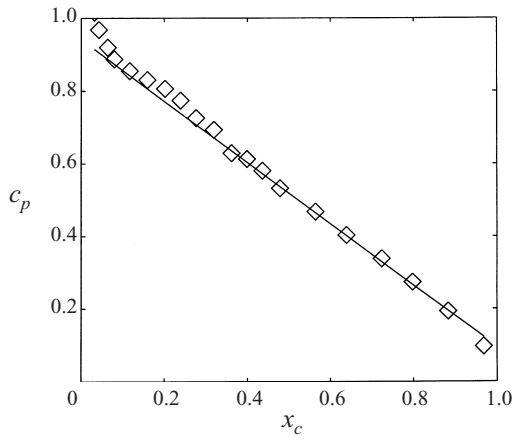

FIGURE 4. Experimental and analytical pressure distribution for the swept-wedge flow (◇, Müller & Bippes 1988).

		Chordwise length	Domain length	Grid
(*a*)	Box 1	$0.20 < x_c < 0.36$	$358 \times 50 \times 108$	$326 \times 49 \times 33$
	Box 2	$0.36 < x_c < 0.54$	$386 \times 50 \times 108$	$461 \times 61 \times 49$
(*b*)	Box 1	$0.20 < x_c < 0.32$	$272 \times 50 \times 108$	$266 \times 49 \times 33$
	Box 2	$0.32 < x_c < 0.5$	$386 \times 50 \times 108$	$461 \times 61 \times 49$
(*c*)	Box 1	$0.20 < x_c < 0.32$	$272 \times 50 \times 36$	$266 \times 49 \times 33$
	Box 2	$0.32 < x_c < 0.5$	$386 \times 50 \times 36$	$921 \times 61 \times 49$

TABLE 1. Computational parameters for (*a*) LOW-T, (*b*) HIGH-T and (*c*) HIGH-TF cases.

blowing (random time-dependent disturbances) was set to $A_t = 10^{-4}$ for LOW-T and $A_t = 10^{-2}$ for HIGH-T and HIGH-TF. By choosing an order-of-magnitude difference in the unsteady components, stationary-vortex-dominated transition can be compared with transition resulting from travelling vortices.

Recall that the outflow boundary treatment involved a portion of the computational domain, the buffer region. For all simulations, a fixed chordwise length $107\delta_0$ (equivalent to a chord length $\Delta x_c = 0.05$) was used for the buffer regions.

Figure 1(*b*) showed the various coordinate systems used for the swept-wing problem. Although the equations are solved in the body-oriented coordinate system (x, y, z) or (x_c, y_c, z_c), most of the results are presented in the flow-oriented coordinate system (x_s, y_s, z_s), which denotes tangent, wall-normal, and perpendicular directions to the local external streamline.

4.2. *Local characteristics of the flow field*

Streamwise mean and disturbance velocities for the LOW-T simulation are shown in figures 5–7. Figures 5 and 6 show that velocity contours of the mean and disturbance components, respectively, in spanwise/wall-normal (y, z) planes are parallel to the leading edge of the swept wedge. At $x_c = 0.3$, the amplitude of the crossflow vortices are still relatively small, and the mean flow is unaffected by the disturbances. Near $x_c = 0.35$, the presence of the crossflow vortices becomes detectable in the mean flow. After $x_c = 0.40$, the results in figure 5 indicate that the mean flow becomes significantly altered by the crossflow disturbances. The vortex roll-over (or half-

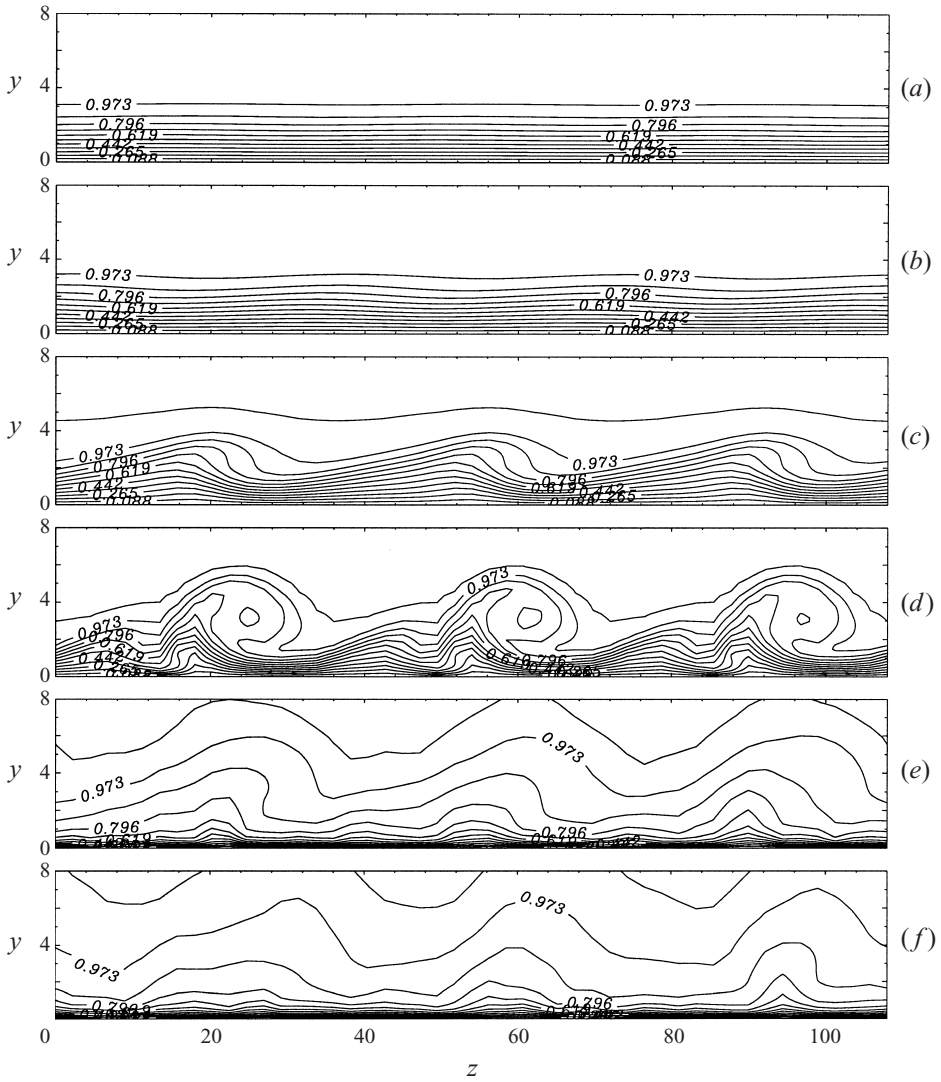

FIGURE 5. Contours of the time-averaged mean streamwise velocity U_s for the LOW-T case. (*a*) $x_c = 0.3$; (*b*) $x_c = 0.35$; (*c*) $x_c = 0.4$; (*d*) $x_c = 0.42$; (*e*) $x_c = 0.45$; (*f*) $x_c = 0.5$. The vertical scale is amplified for clarity.

mushroom structure) is clearly visible in both figures 5 and 6 between $x_c = 0.40$ and $x_c = 0.45$. Figure 6 shows weak secondary crossflow vortices relatively close to the wall at $z \approx 10$, 46 and 82, with the same wavelength as the dominant stationary-vortex component. Malik *et al.* (1994) also observed secondary instabilities in their numerical study. Figure 7 shows the streamwise mean velocity profiles as a function of the distance from the wall at various streamwise locations and at four spanwise locations. These results indicate that doubly inflectional velocity profiles occur in the same region as the half-mushroom structure.

Figures 8 to 10 show streamwise mean and disturbance velocities for the HIGH-T case. Up to $x_c \simeq 0.35$ the evolutionary features of the crossflow disturbance for the LOW-T and HIGH-T are very similar. Beyond $x_c = 0.35$, however, the distinct roll-over

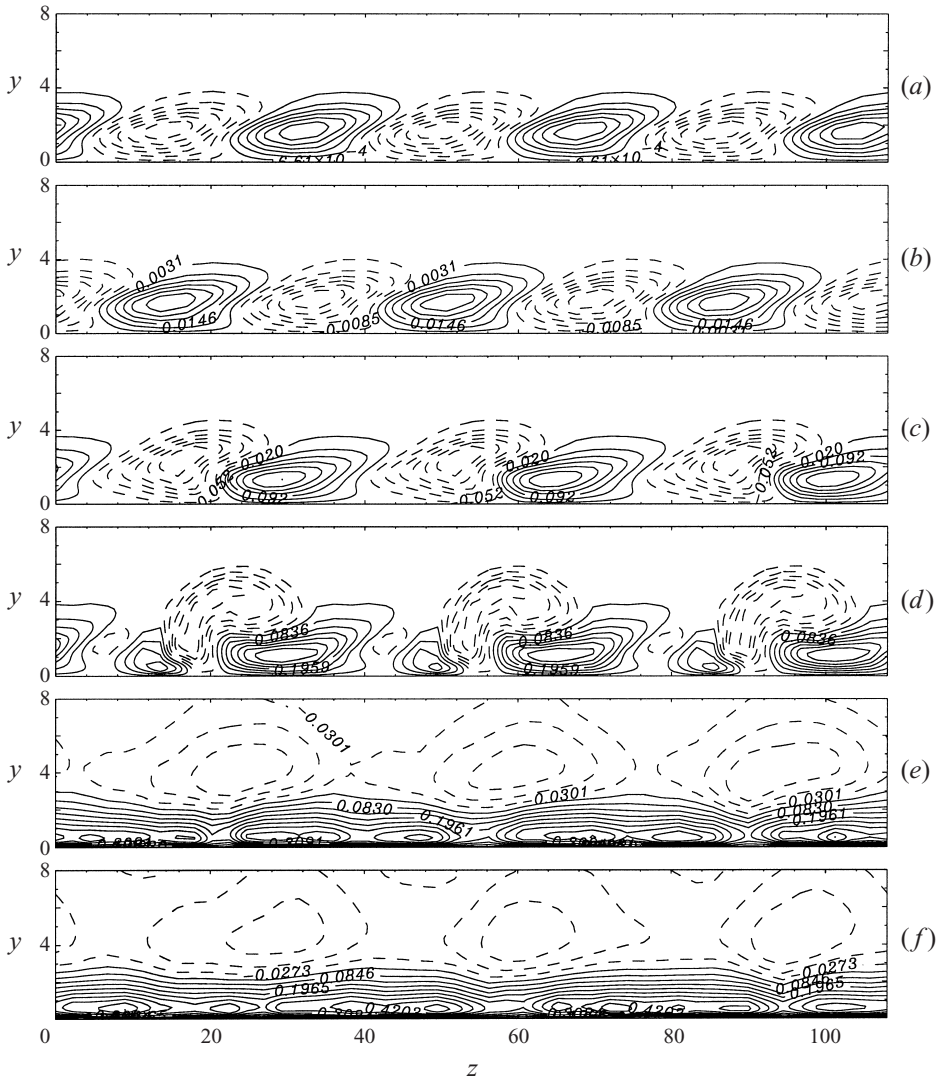

FIGURE 6. Contours of the time-averaged streamwise disturbance velocity $\widetilde{u}_s$ for the LOW-T case. (*a*) $x_c = 0.3$; (*b*) $x_c = 0.35$; (*c*) $x_c = 0.4$; (*d*) $x_c = 0.42$; (*e*) $x_c = 0.45$; (*f*) $x_c = 0.5$. The vertical scale is amplified for clarity.

structure, secondary vortices, and strong doubly inflectional velocity profiles described above are not observed in the HIGH-T case. It appears, in this case, that the high-speed fluid remains near the wall and the low-speed fluid diffuses just prior to the roll-over event found in LOW-T. Correspondingly, the velocity profiles (figure 10) in the HIGH-T case exhibit only marginal inflection points.

The present results for the LOW-T case matched the previous stationary-crossflow-dominated transition studies of Dagenhart (1992), Meyer & Kleiser (1988), Malik *et al.* (1994), and Joslin & Streett (1994). The HIGH-T results, which involve both stationary and travelling crossflow vortices, however, are substantially different. They suggest that the strength of the stationary vortex is linked to vortex roll-over; with travelling disturbances competing for energy, the stationary modes are robbed of the

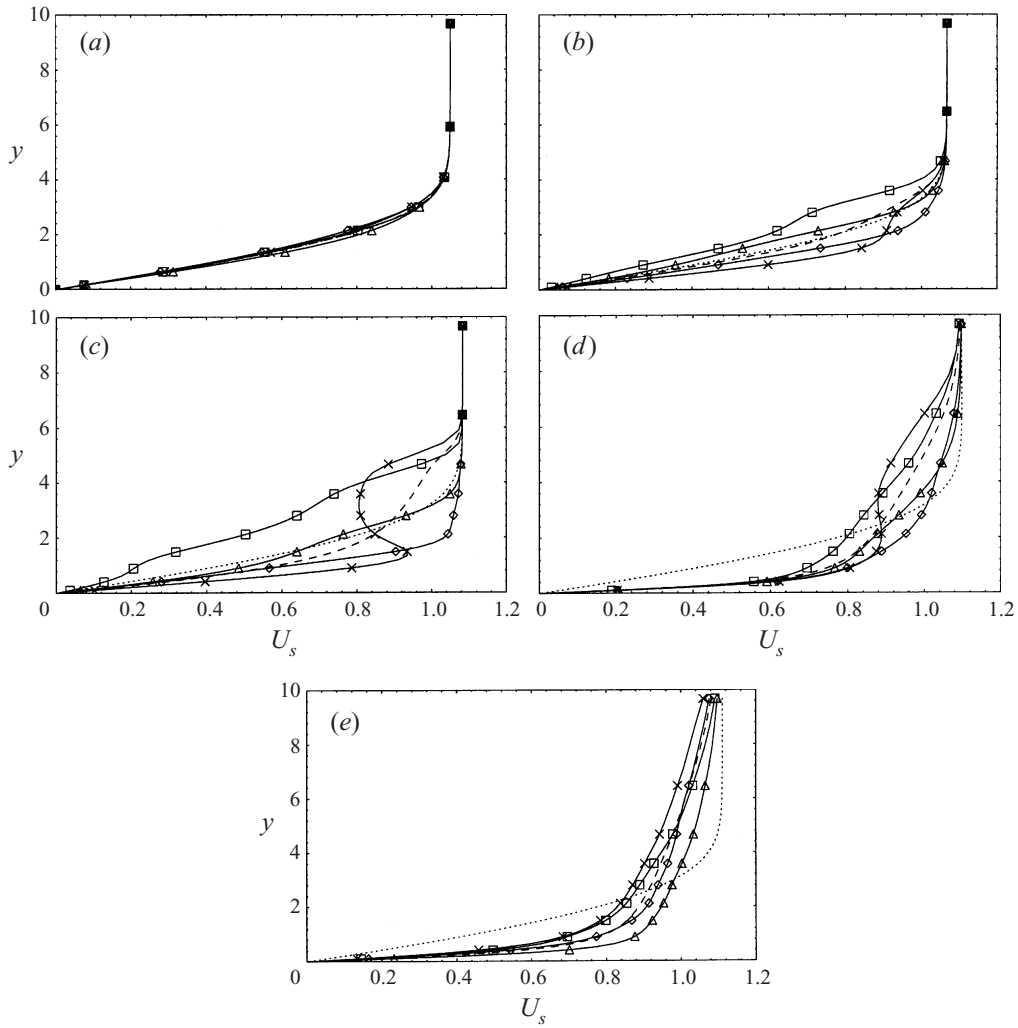

FIGURE 7. Wall-normal profiles of the time-averaged streamwise mean velocity U_s for LOW-T. (*a*) $x_c = 0.35$; (*b*) $x_c = 0.4$; (*c*) $x_c = 0.45$; (*d*) $x_c = 0.5$; (*e*) $x_c = 0.54$. ◇, $z = 0$; △, $z = 9$; □, $z = 18$; ×, $z = 27$.

necessary energy, preventing the development of doubly inflectional profiles, as will be further discussed in §4.4.

4.3. *Global characteristics of the flow field*

Contours of mean wall shear are shown in figure 11 (two computational domains are shown side by side in each part). The alternating high- and low-shear regions associated with the crossflow vortices are evident. As in the experiment of Dagenhart (1992), no adjustment of vortex spacing is observed, in contrast to the experimental results of Arnal & Juillen (1987); however, as the vortices evolve and spread with chordwise distance, merging of the vortices occurs due to this natural spreading, as discussed by Joslin & Streett (1994).

The transition location can be estimated in figure 11 as the place where the distinct streak patterns become blurred or disappear. For LOW-T and HIGH-T they are at

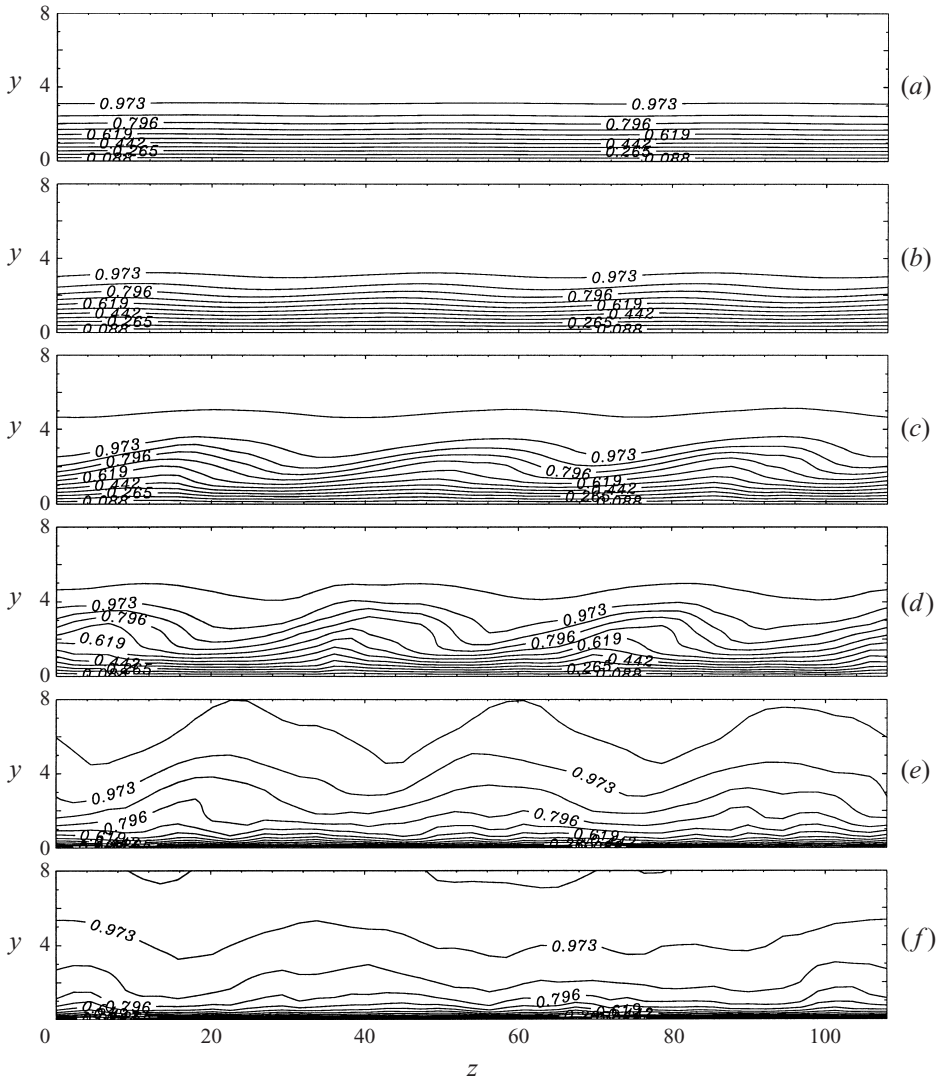

FIGURE 8. Contours of the time-averaged mean streamwise velocity U_s for the HIGH-T case. (*a*) $x_c = 0.3$; (*b*) $x_c = 0.35$; (*c*) $x_c = 0.4$; (*d*) $x_c = 0.42$; (*e*) $x_c = 0.45$; (*f*) $x_c = 0.5$. The vertical scale is amplified for clarity.

$x_c \simeq 0.45$ and 0.42 respectively. Transition occurs earlier in the higher time-dependent disturbance (HIGH-T) case. This result is consistent with the experimental results of Müller & Bippes (1988), who suggested that the travelling waves play the most important role in determining the onset of transition, while large amplitudes of the stationary vortices do not seem to advance transition. Another interesting observation is that in the LOW-T case the change of the streak patterns in the downstream region is milder and remnants of the stationary vortices extend deep into the transition and turbulent regions, as discussed above.

Other indications of boundary-layer transition can be assessed by computing the displacement thickness δ_s^*, momentum thickness θ_s, shape factor H_s and skin-friction coefficient $C_{f,s}$ associated with the streamwise mean velocity U_s. These global quanti-

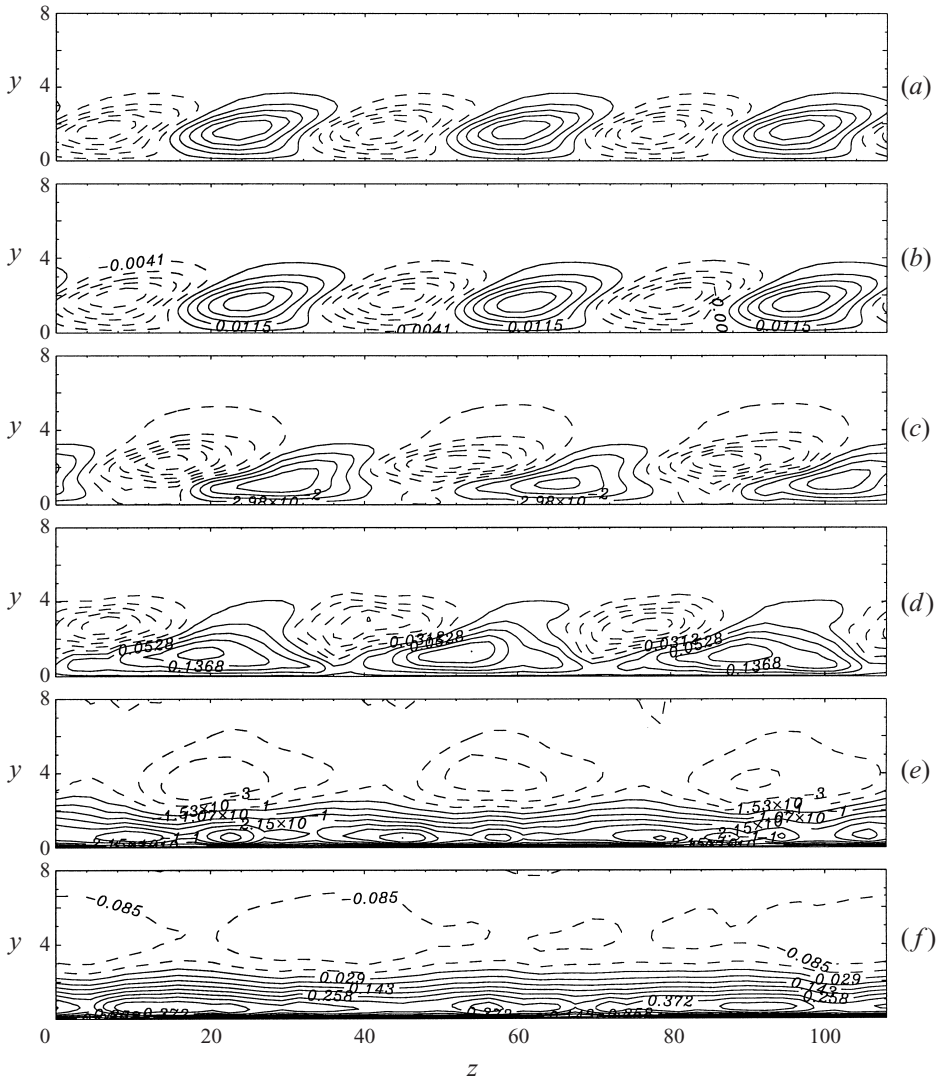

FIGURE 9. Contours of the time-averaged streamwise disturbance velocity $\widetilde{u}_s$ for the HIGH-T case. (*a*) $x_c = 0.3$; (*b*) $x_c = 0.35$; (*c*) $x_c = 0.4$; (*d*) $x_c = 0.42$; (*e*) $x_c = 0.45$; (*f*) $x_c = 0.5$. The vertical scale is amplified for clarity.

ties are defined in the streamline coordinate system as

$$\delta_s^* = \int_0^{y_{max}} \left(1 - \frac{U_s}{U_{e,s}}\right) \mathrm{d}y, \quad \theta_s = \int_0^{y_{max}} \frac{U_s}{U_{e,s}} \left(1 - \frac{U_s}{U_{e,s}}\right) \mathrm{d}y, \tag{4.2}$$

$$H_s = \frac{\delta_s^*}{\theta_s}, \quad C_{f,s} = \frac{2\tau_{w,s}}{\rho U_{e,s}^2}, \tag{4.3}$$

where $U_{e,s}$ is the streamwise boundary-layer edge velocity and capital letters denote time-averaged quantities.

Figure 12 shows the chordwise variation of the skin-friction coefficient and shape factor for the LOW-T, HIGH-T and HIGH-TF cases. Consistent with the velocity contours

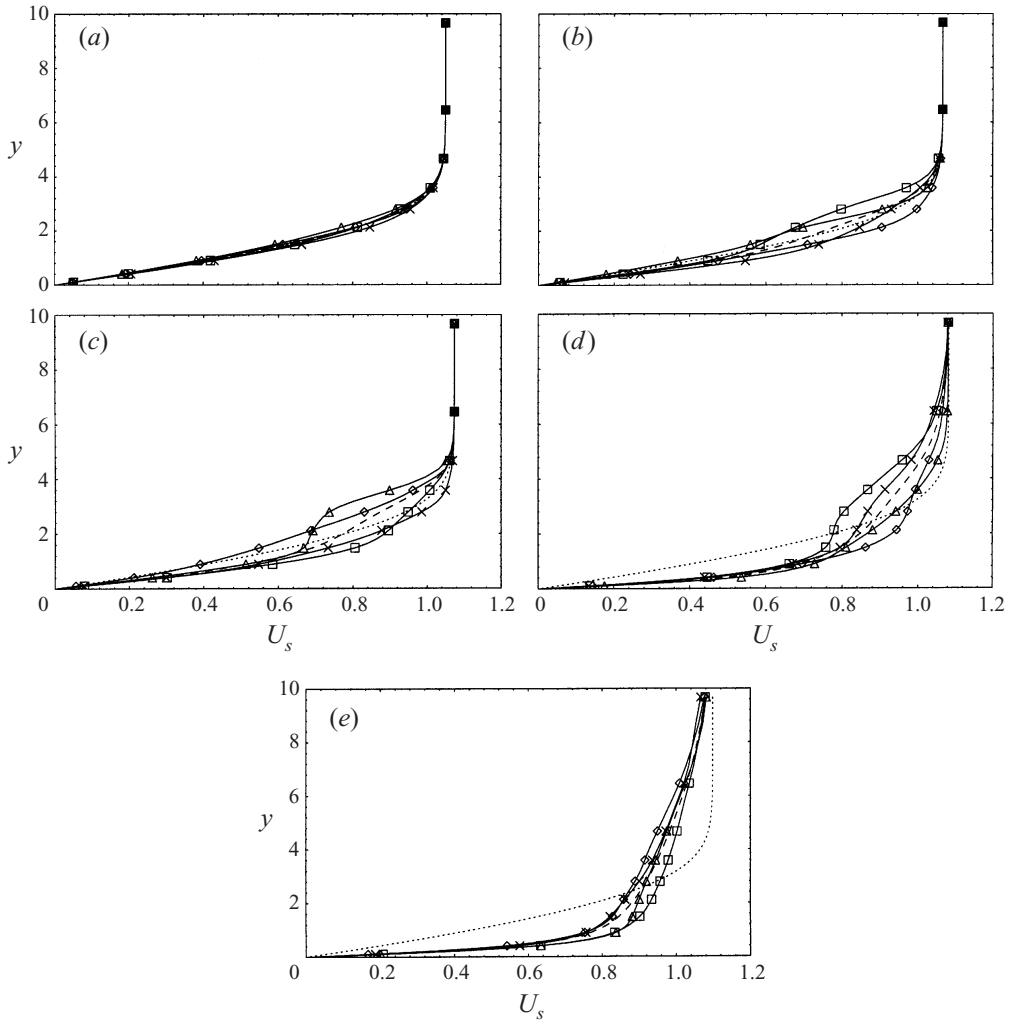

FIGURE 10. Wall-normal profiles of the time-averaged streamwise mean velocity U_s for HIGH-T. (*a*) $x_c = 0.35$; (*b*) $x_c = 0.4$; (*c*) $x_c = 0.42$; (*d*) $x_c = 0.45$; (*e*) $x_c = 0.5$. ◇, $z = 0$; △, $z = 9$; □, $z = 18$; ×, $z = 27$.

(figures 5 and 8), the initial amplification of the disturbances does not alter the mean laminar flow state. As the amplitude of the crossflow disturbances becomes finite, the mean flow becomes distorted and the nonlinear transition process commences. The skin friction coefficient C_f increases rapidly and the shape factor H decreases from laminar to transitional to turbulent values. Finally, the friction and shape-factor values indicate that a nearly turbulent state is being approached by the end of the simulations.

A comparison between HIGH-T and HIGH-TF results indicates that the HIGH-T grid is insufficiently resolved. Refining the grid results in an earlier breakdown of the laminar flow, as evidenced by the fact that the skin-friction coefficient begins to rise at $x_c = 0.40$ and 0.42 in the finer and coarser calculations, respectively. Computational resources, however, were quickly exhausted and no further grid refinement could be run. Although grid-invariance of the results was not achieved, and quantitative

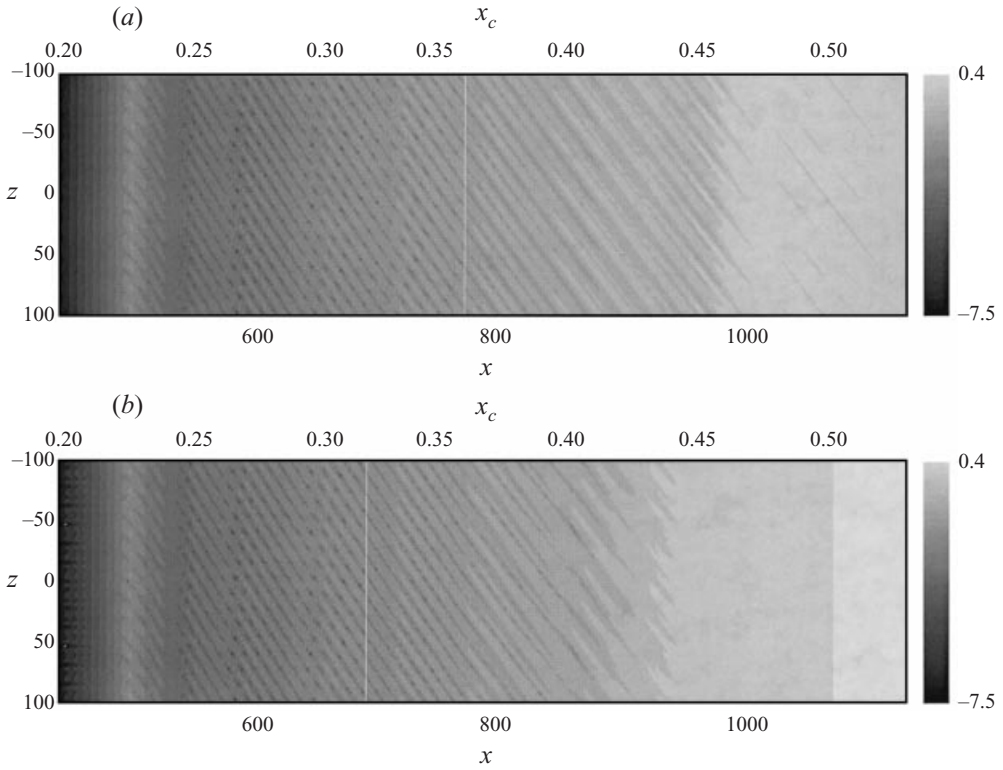

FIGURE 11. Contours of mean wall shear $\log_{10}(\partial V/\partial y)_w$. (*a*) LOW-T; (*b*) HIGH-T. The white vertical lines represent the junction between the first and the second boxes.

differences can be observed between the simulations HIGH-T (coarser) and HIGH-TF, the qualitative features obtained are fairly grid-independent, as will be shown later.

Owing to both the sweep angle of the model and the pressure gradient, the streamlines and wall shear stress change direction with chordwise location. As shown by Meyer & Kleiser (1988) and Joslin & Streett (1994), the crossflow vortices are aligned within a few degrees of the external streamwise direction. The angles obtained by measuring the streak patterns in the present study are shown in figure 13. The LES results show a deviation of $\varepsilon = 4^\circ$ from the streamline direction (denoted by β), which is within the range of previous results, $\varepsilon = 3^\circ$–5° (Nitschke-Kowsky & Bippes 1988). The wall shear stress initially follows the laminar base-state direction, as expected; however, as transition occurs, the strength of the crossflow disturbances dominates the near-wall flow, and the shear direction switches from the laminar state to the direction of the crossflow vortex disturbance. This realignment persists into the turbulent boundary layer.

The mean velocity profiles in wall units near the end of the second box of the various simulations are plotted in figure 14, together with the linear profile $U^+ = y^+$ and the logarithmic law $U^+ = \ln y^+/0.41 + 5.2$. A long logarithmic layer with the slope of 1/0.41 is evident, but is clearly shifted upward from the two-dimensional log-law. This indicates a thickening of the near-wall layer, and may be due either to physical causes or to insufficient grid resolution. A significant decrease of the log-layer intercept is in fact obtained by refining the mesh. It should be remarked that in the turbulent-like region of the HIGH-TF simulation the grid size in wall units

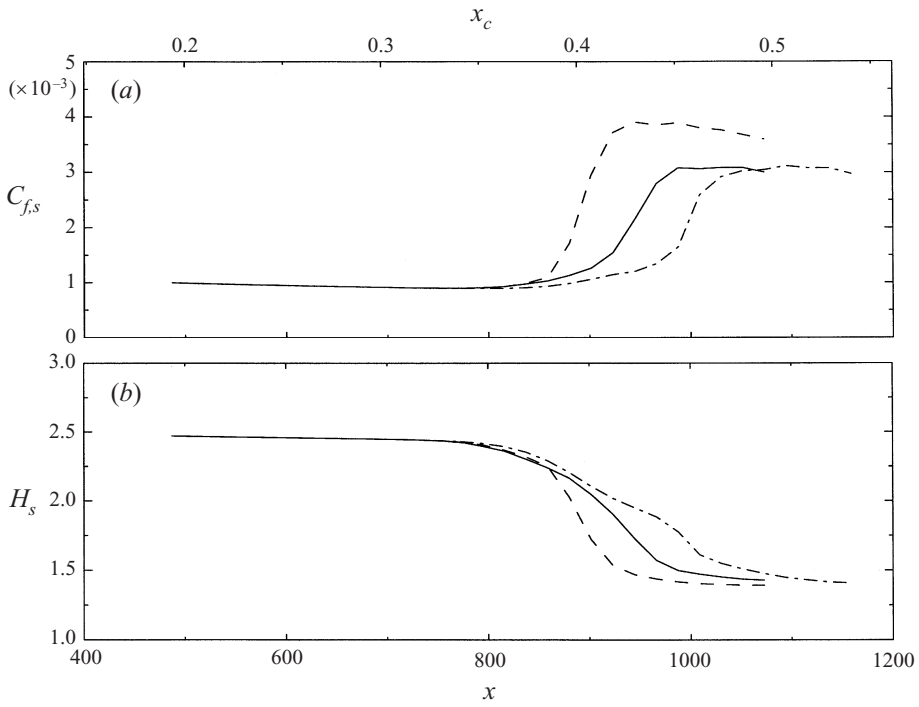

FIGURE 12. Chordwise variation of the (*a*) skin friction coefficient and (*b*) shape factor. —·—, LOW-T; ——, HIGH-T; – – –, HIGH-TF.

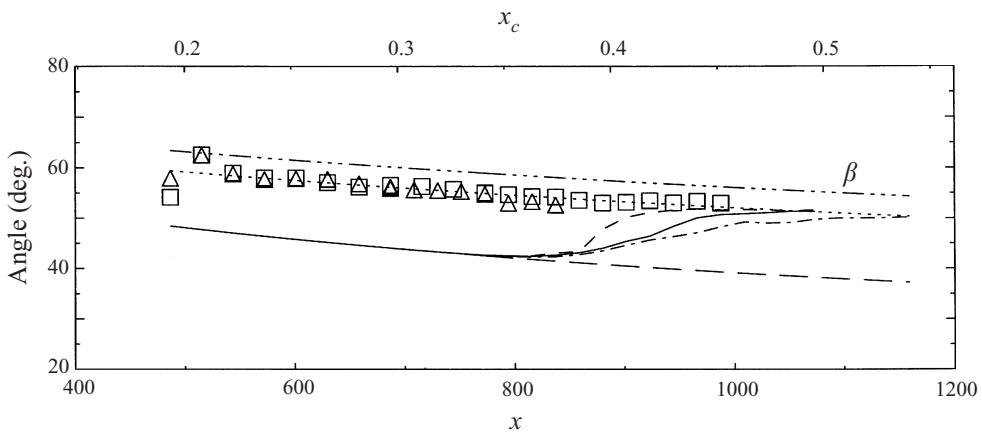

FIGURE 13. Angle of the crossflow disturbance propagation. Stationary crossflow vortex angle $\beta - \varepsilon$: □, LOW-T; △, HIGH-T; ·····, $\beta - 4°$. Wall shear stress angle: ————, laminar base flow; —·—, LOW-T; ——, HIGH-T; – – –, HIGH-TF.

is $\Delta x^+ = 23$, $\Delta y^+_{min} = 0.27$, $\Delta z^+ = 42$, which, in the coordinate system aligned with the wall stress gives $\Delta x^+_s = 46$ and $\Delta z^+_s = 23$. The LES of a turbulent flat-plate boundary layer that used the same grid resolution gave mean velocity profiles in very good agreement with the DNS results (Huai *et al.* 1997), with a logarithmic layer with the correct intercept. Based on this consideration, the fact that, with the same effective grid resolution, the three-dimensional boundary layer has a thicker near-wall

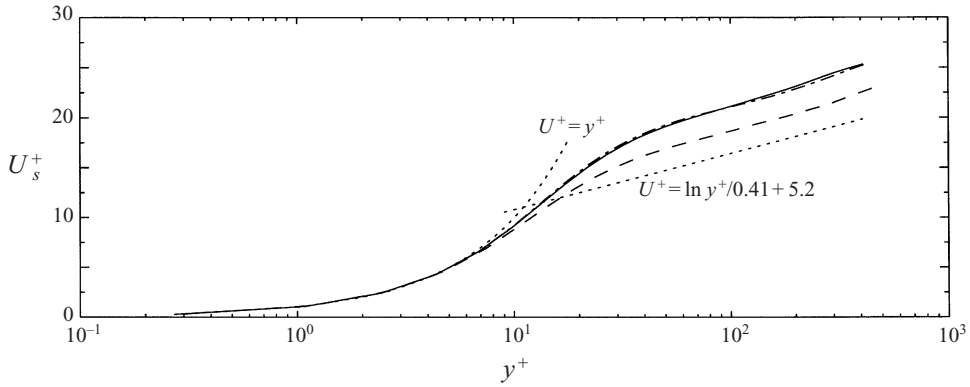

FIGURE 14. Spanwise-averaged chordwise velocity distribution in the turbulent region. ——, LOW-T; —·—, HIGH-T; – – –, HIGH-TF.

layer seems to be due mostly to physical reasons. It can be due partly to the fact that fully developed turbulent flow has not been achieved prior to the end of the computational domain, but it may be also an effect of the presence of the stationary crossflow vortices. High values of the log-layer intercept had been previously found in other simulations involving vortex-dominated flows (Liu, Piomelli & Spalart 1996).

4.4. *Spectral analysis*

Next, the spanwise wavenumber spectra of the steady streamwise perturbation velocity were calculated. Figure 15 gives the maximum amplitude of each spanwise mode with chordwise location for LOW-T, HIGH-T and HIGH-TF, obtained from

$$A_{max}(x, k_z) = \max[A(x, y, k_z)], \quad y \in [0, \ y_{max}], \tag{4.4}$$

where $A(x, y, k_z)$ is the magnitude of spanwise mode k_z at point (x, y). Because the forced dominant stationary mode has three periods over the spanwise length of the box L_z, the wavenumber of the primary crossflow mode (denoted by k_z) satisfies the relationship $k_z L_z/2\pi = 3$. We denote this dominant wavelength as λ_3. In the LOW-T case shown in figure 15(*a*) the primary crossflow mode λ_3 reaches an amplitude equal to 28% of the free-stream inflow velocity prior to transition. The harmonic with one-half the wavelength of the dominant mode, $\lambda_3/2$, attains the peak magnitude of 18%, while $\lambda_3/3$ reaches about 10%. It is also evident that the energy cascade appears in the harmonics of the primary wave and not in its subharmonics. The emergence of energy in the harmonics and not subharmonics is consistent with the experiments of Reibert & Saric (1997). Furthermore, this cascade of energy suggests that the growth of higher harmonics can be attributed to a fundamental secondary instability (the crossflow mode with one-half the wavelength of the dominant mode) as discussed by Reed (1987). Similarly to the previous experiments and DNS, saturation of the stationary vortices is observed prior to transition. Huai (1996) found a high growth rate of secondary instability for the travelling modes during the saturation process of the stationary vortices. In the HIGH-T and HIGH-TF cases, shown in figures 15(*b*) and 15(*c*), the harmonics of the dominant mode never amplify as in the LOW-T case; the primary wave only reaches an energy level of 14% of the free-stream inflow velocity. Evidently, with higher unsteady components in the flow, the secondary modes are not encouraged to amplify. Very little difference can be observed between the HIGH-T

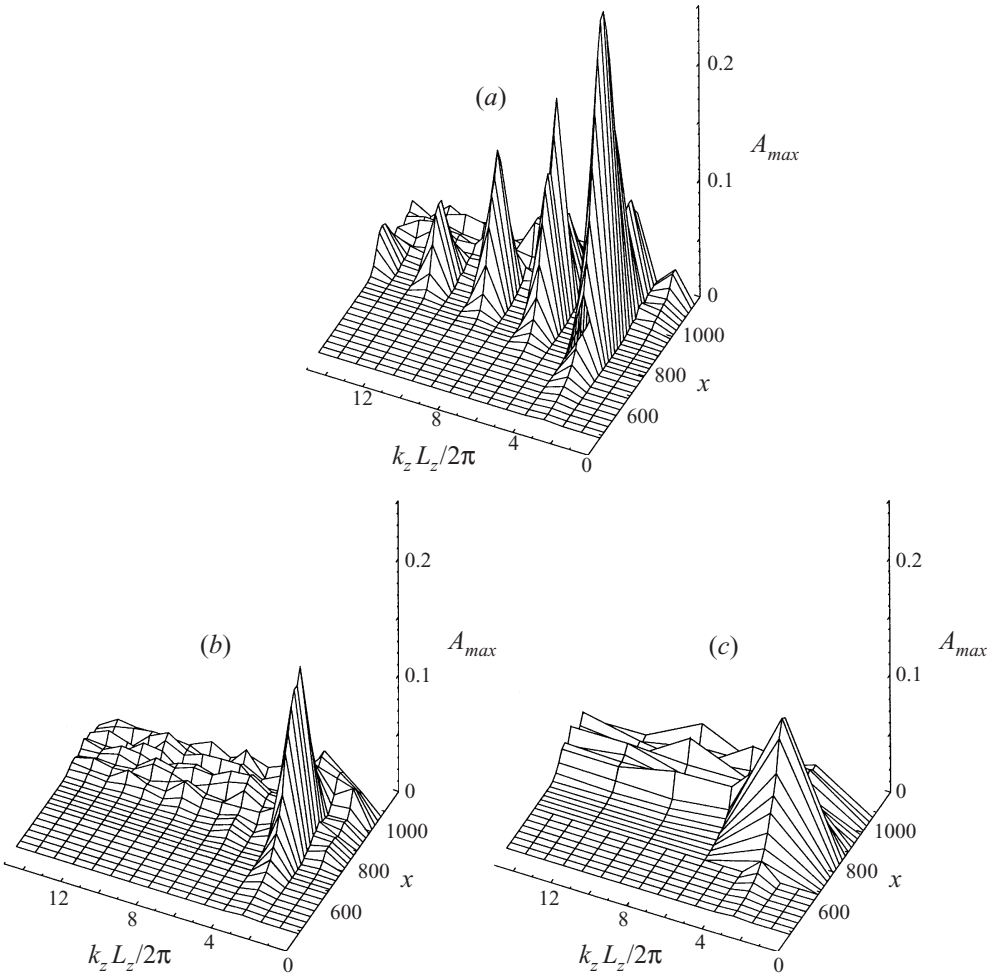

FIGURE 15. Chordwise development of the spanwise-wavenumber spectrum. (*a*) LOW-T; (*b*) HIGH-T; (*c*) HIGH-TF.

and HIGH-TF results, apart from an earlier growth of the λ_3 mode in the coarser computation.

The chordwise growth of several harmonics of the perturbation velocity and the zeroth-wavenumber mode are shown in figure 16. In the LOW-T case, the primary mode (λ_3) grows exponentially (with an amplification rate $\alpha_i \simeq 11$ in good agreement with the experimental results of Müller & Bippes 1988) and initially has the largest energy content, since it is generated by the steady suction and blowing. The harmonics $\lambda_3/2$ and $\lambda_3/3$ grow with amplification rates of $\alpha_i \simeq 24$ and $\alpha_i \simeq 39$, as would be expected from direct harmonics of the primary mode. At $x_c = 0.39$, the primary mode starts to saturate and reaches a peak amplitude 28% at $x_c = 0.41$; the second harmonic saturates at approximately the same location, while the saturation of the third harmonic occurs downstream of the first- and second-mode saturation point. The mean velocity mode also shows the tendency to saturation when the primary mode saturates, but it regains exponential growth as the transition zone is entered and the unsteady modes begin to dominate the transition process. At the transition

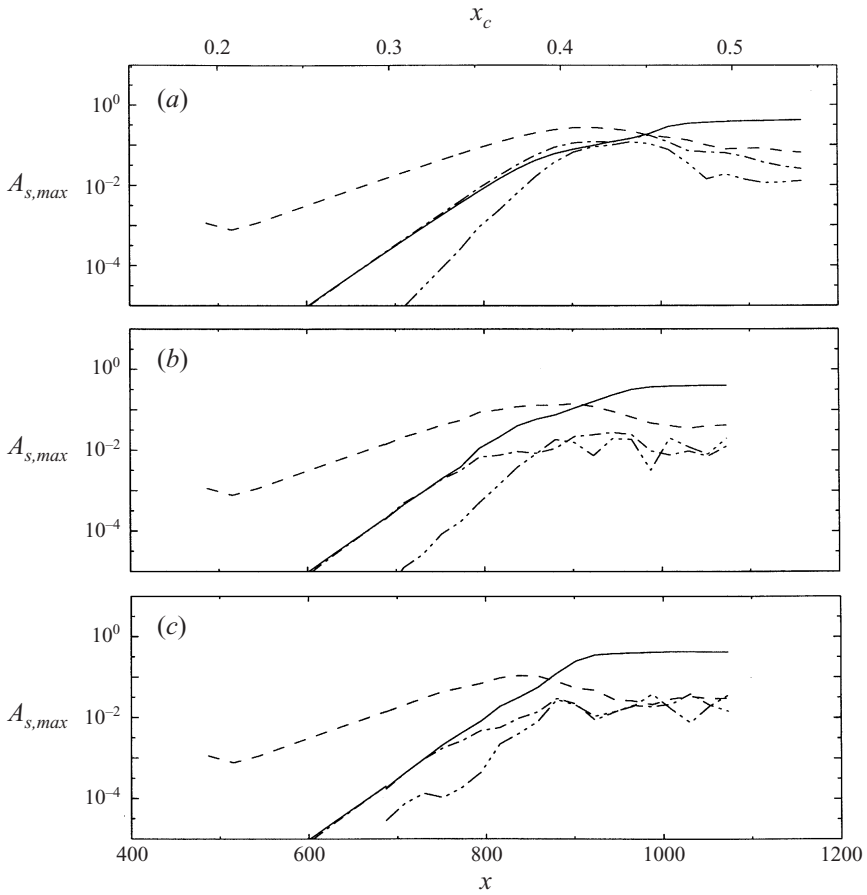

FIGURE 16. Chordwise development of the dominant stationary modes. (*a*) LOW-T; (*b*) HIGH-T; (*c*) HIGH-TF. ——, Mean velocity; – – –, λ_3 mode; —·—, $\lambda_3/2$ mode; —···—, $\lambda_3/3$ mode.

location $x_c = 0.45$, all the modes have amplitudes of the same order of magnitude. In the HIGH-T and HIGH-TF cases, the primary mode and the second harmonic have the same initial growth rates as in the LOW-T case, but, at the transition location, they have less energy by roughly one order of magnitude. The distortion of the mean flow follows the growth of the second harmonic up to the saturation point. Again, the HIGH-T and HIGH-TF results are in very good qualitative agreement, the main difference being the earlier growth of λ_3 observed before, while the higher harmonics are in good quantitative agreement. In the PSE computations of Malik *et al.* (1994), a travelling-mode-dominated case led to growth of temporal and spatial harmonics of the primary mode.

Finally, the frequency spectra of the streamwise fluctuation velocity u_s are shown in figure 17 for the LOW-T and HIGH-T cases. When the amplitude of the travelling modes is low, a low-frequency band centred at $f \simeq 90$ Hz begins to amplify, in agreement with the prediction of linear stability theory and experiments (see Bippes *et al.* 1991). At $x_c = 0.35$, however, a second peak is observed in the spectrum at approximately 180 Hz, corresponding to the amplification of the harmonic of the primary travelling wave. The travelling disturbances are dominated by the low-frequency band until $x_c = 0.4$, but at $x_c = 0.45$ a high-frequency band with frequencies one order of

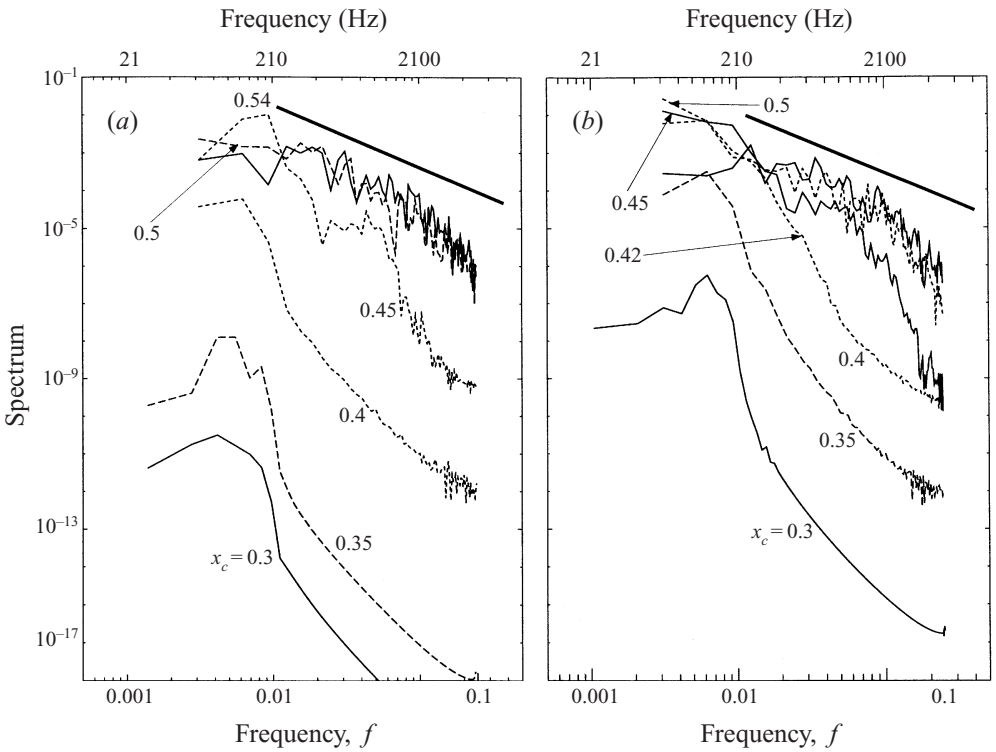

FIGURE 17. Spectrum of the streamwise velocity disturbance $\widetilde{u}_s$ at the maximum travelling-wave location. (*a*) LOW-T case, (*b*) HIGH-T case. The thick line denotes a $-5/3$ slope.

magnitude higher is strongly amplified, in agreement with the findings of Kohama *et al.* (1991), and the peak in the spectrum moves to the second harmonic. In the transition and turbulent regions, the distribution of the spectrum becomes closer to that of a turbulent flow; about four decades of the spectrum are resolved. It is not clear from this comparison what drives the flow through the transition region to the turbulent state; however, the present results do not contradict the proposition by Kohama, Onodera & Egami (1996), who claimed that, in this situation, the secondary mode drives the flow to turbulence. Figure 17(*b*) shows the frequency spectrum for the HIGH-T case. A shift of the peak low-frequency mode occurs at $x_c = 0.4$; however, the high-frequency band is not prominent at the transition location ($x_c = 0.42$); the secondary instability associated with the inflectional points is much weaker because the stationary vortex has less energy and only marginal inflection points are observed in the velocity profiles. The travelling modes play a more significant role in the transition process for the HIGH-T case.

5. Conclusions

The spatial evolution of crossflow disturbances in a swept-wedge boundary layer was computed using the large-eddy simulation (LES) approach with the primary goals of studying the flow physics associated with stationary and travelling crossflow vortex interactions and evaluating the effectiveness and limits of using LES as a tool for the prediction of boundary-layer transition in a complex three-dimensional flow.

For stationary-crossflow-dominated transition (LOW-T), results from the present

simulations are consistent with the flow processes previously documented using wind-tunnel experiments and direct numerical simulations (DNS). Initially, the disturbances approximately align with the direction of the external streamline, forming a 4° differential angle with the streamline (consistent with linear theory). As the disturbances are amplified, spanwise planes of streamwise velocity contours showed the evolution from a wave-like structure to the vortex-roll-over or half-mushroom structure. Within this half-mushroom structure, doubly inflectional velocity profiles are present just prior to the onset of boundary-layer transition. The inflection points lead to amplification of high-frequency secondary instability, followed by a rapid filling of the spectrum and transition within a few percent chord downstream of the inflectional profiles. The transition locations predicted from the streak patterns agreed with predictions using the streamwise skin-friction coefficient. In this study we observed the amplification of harmonic modes of the primary disturbance, while no energy was found in any subharmonic modes (a recently published experiment (Reibert *et al.* 1996) confirms this finding). The present use of LES has enabled the first spatial simulation of the complete transition process from the onset of stationary crossflow disturbances and small-amplitude travelling modes, to secondary instability, to transition to turbulence.

Previous wind-tunnel experiments and temporal DNS studied the interaction of stationary and discrete travelling disturbances. The present HIGH-T simulation yields the first study of the interaction of stationary disturbances and high-amplitude random travelling disturbances from initiation through transition to turbulence. For the higher-amplitude travelling disturbance case (HIGH-T), the results showed that during the initial evolution the disturbances are also approximately aligned in the direction of the external streamline (4° differential angle). The disturbances amplify, interact, and induce boundary-layer transition. For the HIGH-T case, the half-mushroom structure is not observed in the simulation, the growth of energy is suppressed for the higher-harmonic modes, and the secondary instability is not dominant. However, similarly to the LOW-T case, the transition locations predicted from the streak patterns agreed with predictions using the streamwise skin-friction coefficient. The travelling disturbances have a stronger role in the transition process compared with LOW-T, where secondary instabilities dominate.

While the gross features of the stationary-dominated flow were consistent with previous wind-tunnel and DNS studies, the HIGH-T and HIGH-TF comparison indicates that the issue of grid independence was not completely resolved. Although the qualitative trends and some of the quantitative predictions obtained with these simulations match well, other quantities had not reached grid-invariance.

This work was sponsored by the NASA Langley Research Center under grant NAG 1-1089. The computer resources were provided by the Numerical Aerodynamic Simulation Facility. The authors thank the referees for their insightful comments.

REFERENCES

ARCARA, P. C. JR., BARTLETT, D. W. & MCCULLERS, L. A. 1991 Analysis for the application of hybrid laminar flow control to a long-range subsonic transport aircraft. *SAE Paper* 912113.

ARNAL, D., COUSTOLS, E. & JUILLEN, J. C. 1984 Experimental and theoretical study of transition phenomena on an infinite swept wing. *La Rech. Aéro.* **4**, 39–54.

ARNAL, D. & JUILLEN, J. C. 1987 Three-dimensional transition studies at ONERA/CERT. *AIAA Paper* 87–1335.

BALACHANDAR, S., STREETT, C. L. & MALIK, M. R. 1990 Secondary instability in rotating disk flow. *AIAA Paper* 90–1527.

Bertolotti, F. P. & Crouch, J. D. 1992 Simulation of boundary-layer transition: receptivity to spike stage. *NASA CR*-191413.

Bippes, H., Müller, B. & Wagner, M. 1991 Measurements and stability calculations of the disturbance growth in an unstable three-dimensional boundary layer. *Phys. Fluids* A **3**, 2371–2377.

Bippes, H. & Nitschke-Kowsky, P. 1987 Experimental study of instability modes in a three-dimensional boundary layer. *AIAA Paper* 87–1336.

Chorin, A. J. 1968 Numerical solution of the Navier-Stokes equations. *Math. Comput*. **22**, 745–762.

Cooke, J. C. 1950 The boundary layer of a class of infinite yawed cylinders. *Proc. Camb. Phil. Soc.* **46**, 645–648.

Dagenhart, J. R. 1992 Crossflow stability and transition experiments in a swept-wing flow. PhD Dissertation, Virginia Polytechnic Institute and State University.

Dagenhart, J. R., Saric, W. S., Hoos, J. A. & Mousseux, M. C. 1990 Experiments on swept-wing boundary layers. Wing. In *Laminar-Turbulent Transition*, vol. III (ed. D. Arnal & R. Michel). Springer.

Dallman, U. & Bieler, H. 1987 Analysis and simplified prediction of primary instability of three-dimensional boundary-layer flows. *AIAA Paper* 87–1337.

Deyhle, H. & Bippes, H. 1996 Disturbance growth in unstable three-dimensional boundary layer and its dependence on environmental conditions. *J. Fluid Mech.* **316**, 73–113.

Falkner, V. M. & Skan, S. W. 1931 Some approximate solutions of the boundary layer equations *Phil. Mag*. **12**, 865–893.

Fischer, T. M. & Dallman, U. 1988 Primary and secondary stability analysis applied to the DFVLR-transition swept-plate experiment. *AGARD-CP*-438, pp. 15.1–15.11.

Gajjar, J. S. B. 1996 On the nonlinear evolution of a stationary cross-flow vortex in a fully three-dimensional boundary layer flow. In *Nonlinear Instability and Transition in Three-Dimensional Boundary Layers* (ed. P. W. Duck & P. Hall), pp. 317–326. Kluwer.

Hall, P., Malik, M. R. & Poll, D. I. A. 1984 On the stability of an infinite swept attachment line boundary layer. *Proc. R. Soc. Lond.* A **395**, 229–245.

Haynes, T. S. & Reed, H. L. 1996 Computations in nonlinear saturation of stationary crossflow vortices in a swept-wing boundary layer. *AIAA Paper* 96-0182.

Huai, X. 1996 Large-eddy simulation of laminar-turbulent transition in spatially developing boundary layers. PhD Dissertation, University of Maryland, College Park.

Huai, X., Joslin, R. D. & Piomelli, U. 1994 Large-eddy simulation of boundary layer transition on swept wings. In *Transition, Turbulence, and Combustion*, vol. I (ed. M. Y. Hussaini, T. B. Gatski & T. L. Jackson), pp. 369–378. Springer.

Huai, X., Joslin, R. D. & Piomelli, U. 1997 Large-eddy simulation of spatial development of transition to turbulence in a two-dimensional boundary layer. *Theor. Comput. Fluid Dyn.* **9**, 149–163.

Itoh, N. 1996 Simple cases of streamline-curvature instability in three-dimensional boundary layers. *J. Fluid Mech.* **317**, 129–154.

Joslin, R. D. 1995 Evolution of stationary crossflow vortices in boundary layers on swept wings. *AIAA J.* **33**, 1279–1285.

Joslin, R. D. & Streett, C. L. 1994 The role of stationary crossflow vortices in boundary-layer transition on swept wings. *Phys. Fluids* **6**, 3442–3453.

Joslin, R. D., Streett, C. L. & Chang, C.-L. 1993 Spatial direct numerical simulation of boundary-layer transition mechanisms: Validation of PSE theory. *Theor. Comput. Fluid Dyn.* **4**, 271–288.

Kachanov, Y. S. 1996 Generation, development and interaction of instability modes in swept-wing boundary layer. In *Nonlinear Instability and Transition in Three-Dimensional Boundary Layers* (ed. P. W. Duck & P. Hall), pp. 115–146. Kluwer.

Kachanov, Y. S. & Levchenko, V. Y. 1984 The resonant interaction of disturbances at laminar-turbulent transition in a boundary layer. *J. Fluid Mech.* **138**, 209–247.

Kachanov, Y. S. & Tararykin, O. I. 1990 The experimental investigation of stability and receptivity of a swept-wing flow. In *Laminar-Turbulent Transition* (ed. D. Arnal & R. Michel), pp. 499–509. Springer.

Kohama, Y., Onodera, T. & Egami, Y. 1996 Design and control of crossflow instability field. In *Nonlinear Instability and Transition in Three-Dimensional Boundary Layers* (ed. P. W. Duck & P. Hall), pp. 147–156. Kluwer.

Kohama, Y., Saric, W. S. & Hoos, J. A. 1991 A high-frequency secondary instability of cross-flow vortices that leads to transition. In *Proc. Boundary-Layer Transition and Control Conf., Peterhouse College, Cambridge, UK*, pp. 4.1–4.13.

Lele, S. K. 1992 Compact finite difference schemes with spectral-like resolution. *J. Comput. Phys.* **103**, 16–42.

Lerche, T. 1996 Experimental investigation of nonlinear wave interactions and secondary instability in three-dimensional boundary-layer flow. In *Advances in Turbulence IV* (ed. S. Gavrilakis, L. Machiels & P. A. Monkewitz), pp. 357–360. Kluwer.

Lingwood, R. J. 1997 On the impulse response for swept boundary-layer flows. *J. Fluid Mech.* **344**, 317–334.

Liu, C. & Liu, Z. 1993 Multigrid direct numerical simulation of the whole process of flow transition in 3D boundary layers. *NASA TM* 106369.

Liu, J., Piomelli, U. & Spalart, P. R. 1996 Interaction between a spatially growing turbulent boundary layer and embedded streamwise vortices. *J. Fluid Mech.* **326**, 151–179.

Malik, M. R., Li, F. & Chang, C.-L. 1994 Crossflow disturbances in three-dimensional boundary layers: nonlinear development, wave interaction, and secondary instability. *J. Fluid Mech.* **268**, 1–36.

Meyer, F. & Kleiser, L. 1988 Numerical investigation of transition in 3D boundary layers. *AGARD-CP*-438, pp. 16.1–16.17.

Meyer, F. & Kleiser, L. 1990 Numerical simulation of transition due to crossflow instability. In *Laminar-Turbulent Transition* (ed. D. Arnal & R. Michel), pp. 609–620. Springer.

Müller, B., Bestek, H. & Fasel, H. 1993 Numerical simulation of the spatial disturbance development in transitional boundary layers along a swept plate. In *Near-Wall Turbulent Flows* (ed. R. M. C. So, C. G. Speziale & B. E. Launder), pp. 869–878. Elsevier

Müller, B., Bestek, H. & Fasel, H. 1996 Nonlinear development of travelling waves in a three-dimensional boundary layer. In *Nonlinear Instability and Transition in Three-Dimensional Boundary Layers* (ed. P. W. Duck & P. Hall), pp. 217–226. Kluwer.

Müller, B. & Bippes, H. 1988 Experimental study of instability modes in a three-dimensional boundary layer. *AGARD-CP*-438, pp. 13.1–13.15.

Nitschke-Kowsky, P. & Bippes, H. 1988 Instability and transition of a three-dimensional boundary layer on a swept flat plate. *Phys. Fluids* **31**, 786–795.

Piomelli, U. & Liu, J. 1995 Large-eddy simulation of rotating channel flows using a localized dynamic model. *Phys. Fluids* **7**, 839–848.

Pruett, C. D., Zang, T. A., Chang, C. L. & Carpenter, M. H. 1995 Spatial direct numerical simulation of high-speed boundary-layer flows – Part I: algorithmic considerations and validation. *Theor. Comput. Fluid Dyn.* **7**, 49–76.

Rai, M. & Moin, P. 1991 Direct numerical simulation of transition and turbulence in a spatially evolving boundary layer. *AIAA Paper* 91-1607.

Reed, H. L. 1987 Wave interactions in swept-wing flows. *Phys. Fluids* **31**, 3419–3426.

Reibert, M. S. & Saric, W. S. 1997 Review of swept-wing transition. *AIAA Paper* 97-1816.

Reibert, M. S., Saric, W. S., Carrillo, R. B., Jr. & Chapman, K. L. 1996 Experiments in nonlinear saturation of stationary crossflow vortices in a swept-wing boundary layer. *AIAA Paper* 96-0184.

Spalart, P. R. 1988 Direct simulation of a turbulent boundary layer up to Re_θ=1410. *J. Fluid Mech.* **187**, 61–98.

Spalart, P. R. 1990 Direct numerical study of crossflow instability. In *Laminar-Turbulent Transition* (ed. D. Arnal & R. Michel), pp. 622–630. Springer.

Streett, C. L. & Macaraeg, M. G. 1989/1990 Spectral multi-domain for large-scale fluid dynamics simulations. *Intl J. Appl. Num. Maths* **6**, 123–140.

Williamson, J. H. 1980 Low-storage Runge-Kutta schemes. *J. Comput. Phys.* **35**, 48–56.